Nanoscale

PAPER

View Article Online
View Journal | View Issue

Cite this: *Nanoscale*, 2024, **16**, 16251

Mesoporous silica–amine beads from blast furnace slag for CO_2 capture applications†

Baljeet Singh, *[a] Marianna Kemell, [a] Juho Yliniemi [b] and Timo Repo *[a]

Received 17th June 2024,
Accepted 8th August 2024

DOI: 10.1039/d4nr02495h

rsc.li/nanoscale

Steel slag, abundantly available at a low cost and containing over 30 wt% silica, is an attractive precursor for producing high-surface-area mesoporous silica. By employing a two-stage dissolution-precipitation method using 1 M HCl and 1 M NaOH, we extracted pure SiO_2, CaO, MgO, *etc*. from blast furnace slag (BFS). The water-soluble sodium silicate obtained was then used to synthesize mesoporous silica. The resulting silica had an average surface area of 100 $m^2\ g^{-1}$ and a pore size distribution ranging from 4 to 20 nm. The mesoporous silica powder was further formed into beads and post-functionalized with polyethyleneimine (PEI) for cyclic CO_2 capture from a mixture containing 15% CO_2 in N_2 at 75 °C. The silica-PEI bead was tested over 105 adsorption–desorption cycles, demonstrating an average CO_2 capture capacity of 1 mmol g^{-1}. This work presents a sustainable approach from steel slag to cost-effective mesoporous silica materials and making CO_2 capture more feasible.

Introduction

In the quest for sustainable development, circular economy principles have gained significant attention in transforming waste into valuable products.[1] This approach addresses the environmental challenges associated with slag and contributes to the design of innovative and more eco-friendly products. By repurposing blast furnace slag (BFS), we can reduce waste, minimize environmental impact, and create sustainable materials that support a greener economy.[2] BFS to produce value-added products such as pure silica, CaO, and MgO, *etc*. creates closed-loop systems and prevents the accumulation of large volumes of waste in landfills. Transforming BFS into porous materials (silica, MOFs, metal oxides, *etc*.) will reduce environmental footprints and contribute to economic growth, fostering a sustainable and resilient future.[3] Various porous functional materials with broad applications can be produced using waste from the steel industry, highlighting the potential for innovative and eco-friendly solutions.[4–6]

In conventional steelmaking, molten pig iron is used to produce steel in a basic oxygen furnace. During this process, raw materials such as dolomite, limestone, and other additives are introduced into the furnace for the production of high-quality steel.[7,8] In 2022, approximately 312 million tons (Mt) of granulated BFS, 104 Mt of air-cooled BFS, 143 Mt of basic oxygen furnace slag, and 68 Mt of electric arc furnace slag were generated worldwide. The gap between slag generated by steel industries and demand is significant. Storing such a large quantity of waste is neither sustainable nor environmentally friendly.[9] Long deposition or storage can also lead to environmental issues, particularly due to the highly alkaline leachates (pH > 11) it produces.[10] Currently, BFS is used in road construction, cement production, and structural construction; however, the demand for other types of slag is very limited.[11]

Hence, methods to recycle slag have been developed and explored for various applications, including metal separation, materials for CO_2 mineralization, catalysts, zeolite synthesis, flue gas desulfurization, *etc*.[12–26] For instance, Kim and colleagues successfully extracted 46% Mg and 35% Al using 2M HCl, while pH control allowed selective separation of 97% Ca.[27,28] BFS was also employed to produce Ca-rich adsorbent materials for CO_2 capture.[29–31] Similarly, Tian *et al.* also utilized slag for CO_2 capture, achieving an enhanced capture capacity of slag-derived adsorbents, exceeding 10 times compared to raw slag, with a maximum uptake of 0.50 g of CO_2 g^{-1} adsorbent.[32] Additionally, Chen *et al.* produced a series of Cu-exchanged zeolite NaX catalysts for selective catalytic reduction of NO_x with NH_3.[33]

Furthermore, Yamashita and co-workers used BFS to produce a layered double hydroxide (LDH) compound through a two-step dissolution-precipitation method and employed LDH as a heterogeneous catalyst for organic transformation.[34] To further advancement of BFS application, Kuwahara *et al.* exploited BFS to synthesize calcium silicate hydrate for wastewater treatment.[35] In another study, Yamashita and colleagues synthesized a mesoporous silica-CaO composite for CO_2

[a]*Department of Chemistry, University of Helsinki, FI-00014 Helsinki, Finland. E-mail: baljeet.singh@helsinki.fi, timo.repo@helsinki.fi*
[b]*University of Oulu, Fibre and Particle Engineering Research Unit, FI-90014, Finland*
† Electronic supplementary information (ESI) available. See DOI: https://doi.org/10.1039/d4nr02495h

capture.[36] With BFS containing significant proportions of Ca (41 wt%), Si (34 wt%), Al (11 wt%), Mg (10 wt%), Ti (0.35 wt%), *etc.*, which can be separated and utilized for various applications with growing market demand, it presents an excellent source of valuable metals.[37–39]

This study aims to extract Si (in the form of sodium silicate) from BFS and utilize it to synthesize mesoporous silica and design silica-supported solid amine beads for CO_2 capture. We designed a 2-stage cyclic dissolution-precipitation method employing 1 M HCl and 1 M NaOH solutions to separate metals and silica (Fig. 1). Furthermore, as synthesized mesoporous silica powder was shaped into beads and post-functionalized by polyethylenimine (PEI) and hexamethylenediamine (HMDA) for CO_2 capture. Overall, this study demonstrates a close circular economy loop by utilizing steel industrial waste to capture CO_2 emissions of the same industrial outlets.

Experimental section

Materials

The chemicals used in this study were analytic grade. Hexamethylenediamine (HMDA), polyethylenimine branched (PEI, MW 25 000), cetyltrimethylammonium bromide (CTAB), and sodium alginate were purchased from Sigma Aldrich and used as received.

Characterization

The surface morphology of the samples was studied using a field emission SEM (Hitachi S-4800). The samples were coated with carbon using a Cressington 108A Carbon coater. Elemental analysis and mapping were performed with an Oxford INCA 350 Energy dispersive X-ray spectrometer connected to the Hitachi S-4800. The EDX spectra were measured at 20 keV. Bruker ALPHA-T FTIR in transmittance mode was used to identify chemical species in samples.

Thermogravimetric analysis (TGA) of samples was conducted using the Mettler-Toledo TGA/DSC-3 + thermal analysis system. The heating rate of 10 °C min^{-1} in a temperature range of 25–600 °C was used under the flow of air (50 mL min^{-1}). The specific surface area and textural properties were measured by N_2 physical adsorption at 77 K using a Quantachrome analyzer.

For CO_2 capture (from 15% CO_2 in N_2), the Mettler-Toledo TGA/DSC-3 + thermal analysis system was used. Initially, samples were activated under the flow of N_2 gas (50 mL min^{-1}) for 15 min. Initially, CO_2 flow was 50 mL min^{-1} (otherwise mentioned), and desorption was performed at 100 °C for 15 min, under N_2 as a sweep gas (flow: 50 mL min^{-1}).

Metals separation. As reported earlier, metals from BFS can be extracted using HCl and precipitated into oxide/hydroxide by adjusting pH using aq. solution of NaOH, known as the dissolution-precipitation method.[40] High-temperature acid dissolution/leaching is a highly effective method to separate metals from silica.[41] Acid dissolve metals including Al, Ca, Mg, *etc.* as [MCl_x] chloride complexes and silica remains unsoluble in 1 M HCl.[42] BFS, 20 g was refluxed at 110 °C in 1 M HCl (250 mL) for 24 h to facilitate dissolution of metals. After 24 h, the insoluble solid was filtered and stored separately. Metals were precipitated by adjusting pH in the range from 8 to 14.

Silica dissolution. To further refine the separation, the solid part (which is mostly nonporous silica) from the acid leaching step was stirred at room temperature in aq. NaOH solution (1 M). During this stage, silica became sodium silicate and soluble in water.

Mesoporous silica synthesis. The sodium silicate solution was separated from the insoluble metal hydroxide and stored for further use. Sodium silicate was then mixed with the CTAB (1 g), and the pH was adjusted to 8 to precipitate silica. After 24 h stirring at room temperature, pure silica is separated and dried.

Spherical silica bead design. Beads were designed using sodium alginate as a binder. A stock solution of sodium alginate was prepared by dissolving 1 mg mL^{-1} in water. While curing solution was prepared by dissolving 188 mg $CaCl_2$ in 30 mL of 0.05 mol L^{-1} polyacrylic acid aq. 1 g silica powder mixed properly with 4 ml sodium alginate solution and suspension was dropped in a curing solution. After shaping, beads were collected, washed with water and ethanol, and dried under vacuum at RT.

Bead functionalization (amine loading). Stock solutions of PEI and HMDA were prepared separately by dissolving 1 g each in ethanol (5 mL) and stored at RT. 200 mg of beads were soaked in stock solution and kept undisturbed for 24 h. Then beads were separated from liquid, washed once with ethanol to remove surface adsorbed imines/amines, and dried under vacuum at RT for 6 h. Silica-PEI and silica-HMDA beads were stored separately at RT and used for further measurements.

Kinetics of CO_2 capture. Three kinetic models were used to access the kinetic parameters of bead and powder samples: Pseudo first order (eqn (1)), Pseudo second order (eqn (2)), and the Avrami kinetic model (eqn (3)).

$$Q_t = Q_e[1 - \exp(-k_1 t)] \quad (1)$$

$$Q_t = k_2 {Q_e}^2 t/(1 + k_2 Q_e t) \quad (2)$$

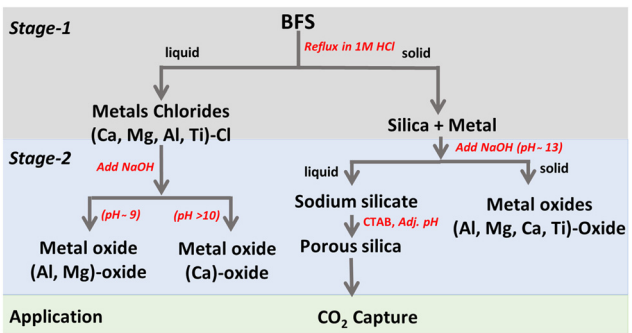

Fig. 1 Illustration of metals and silica separation from BFS.

$$Q_t = Q_e[1 - \exp(-k_A t)^{nA}] \quad (3)$$

where Q_t, and Q_e are the CO_2 capture capacity (mmol g^{-1}) at time t (min) and equilibrium, respectively. k_1 is the Pseudo first order rate constant (min^{-1}), k_2 is the Pseudo second order rate constant (g $mmol^{-1}$ min^{-1}), and k_A is the Avrami rate constant (min^{-1}), and n_A is the order of Avrami model.

Results and discussion

Separation of metal and silica

All the experiments were conducted using the same BFS, and the SEM-EDX elemental analysis revealed that BFS contained 7 wt% Mg, 9 wt% Al, 21 wt% Ca, 1 wt% Ti, and 16 wt% Si (Fig. 2 and Table S1, entry 1†). SEM-EDX elemental mapping demonstrated that metals are uniformly distributed throughout the BFS particles (Fig. S1†), while SEM images indicated that slag particle size ranged from 3–20 μm (Fig. S2†). Elemental analysis revealed that the remaining solid mainly consisted of silica with a small amount of undissolved metal oxides such as Al and Mg (Fig. 2 and Table S1, entry 2†).

To precipitate metals, the pH of the aqueous phase was adjusted using 1 M NaOH aq. solution. At pH 8–9, Al and Mg precipitated first, leaving the remaining aqueous phase containing only Ca (Fig. 2 and Table S1, entry 3†). After separating a mixture of metal (Al and Mg) hydroxides, the pH of the remaining aqueous phase was adjusted to 13–14, resulting in precipitation of Ca (confirmed by SEM-EDX analysis) (Fig. 2 and Table S1, entry 4†).

The remaining solid (mostly containing Si) was refluxed to improve separation in an aqueous NaOH solution (pH ~ 14). The highly basic medium slowly hydrolyses the silica network (–Si–O–Si–) to produce sodium silicate.[43–46] During this step, metals tend to precipitate out as corresponding hydroxides [M–$(OH)_x$].[47] Water-soluble sodium silicate was separated from metal hydroxide by filtration, and the filtrate was then used as a Si source for mesoporous silica synthesis.

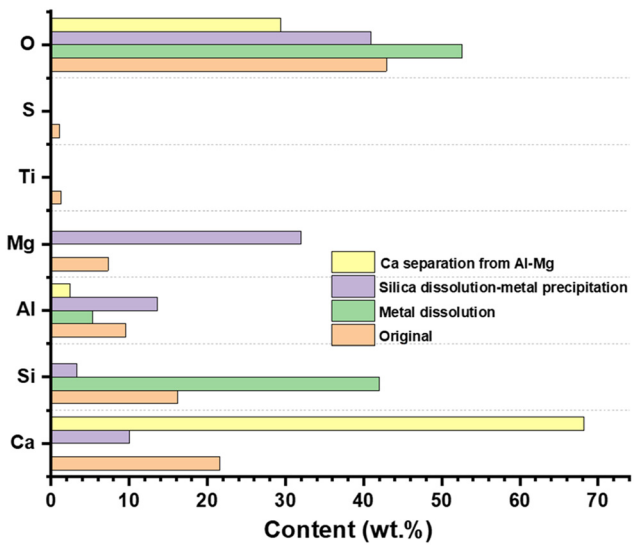

Fig. 2 Chemical composition of original BFS and after dissolution-precipitation of metals and silica.

Synthesis of mesoporous silica. Sodium silicate is a well-known low-cost precursor used for porous silica synthesis.[48–50] Aq. sodium silicate was mixed with CTAB, and pH was adjusted to approximately 8 using 1 M HCl solution. Elemental analysis revealed that the precipitated silica sample contained more than 42 wt% Si with 5 wt% Al (Fig. 1 and Table S2, entry 5†). Mg and Ca were not detected, indicating that the dissolution-precipitation process effectively separated metals and produced pure silica. Elemental mapping also confirmed the uniform distribution of Al-sites within a silica network (Fig. S3†).

SEM image analysis revealed that silica particles were small, with an average size of 300 nm in size and agglomerated (Fig. 3c, d, and S4†). TGA analysis revealed two stages of weight loss. The initial weight loss of approximately 10 wt% (up to 200 °C) could be due to loss of adsorbed gases or moisture in a powder sample. The second stage, involving a weight loss of around 25 wt% between 200 and 600 °C, is attributed to the decomposition and combustion of CTAB, which acted as a structural directing agent in the production of mesoporous silica (Fig. S5†).[51] The silica exhibited a moderate surface area of (100 m^2 g^{-1}) and a wide pore size distribution ranging from 4–20 nm (Fig. S6 and S7†), exhibiting that silica is a mesoporous characteristic. PXRD showed that as-synthesised silica is amorphous (Fig. S8†).

CO_2 capture using amine-functionalized silica bead. The design of CO_2 capture adsorbent is crucial for upscaling and implementing CO_2 capture technology on an industrial level.[52,53] Silica has served as versatile support for designing solid amine adsorbents, with many investigations focusing on powder forms.[54–59] However, for practical industrial applications, low-cost beads or monoliths are preferred over powder.[60,61] In this study, we developed industrial-grade solid amine adsorbents by shaping mesoporous silica powder into micrometer-sized beads (3–4 mm) using sodium alginate as a binder (Fig. S9†).[62–64] N_2 sorption analysis showed that alginate binder had no significant impact on the specific surface area (100 m^2 g^{-1}) (Fig. S10†) and pore size distribution (4–20 nm), although the intensity of larger pores was reduced (Fig. S11†).

Spherical silica beads were post-functionalized with PEI and HMDA, respectively (Fig. S12†), and CO_2 capture capacity was monitored using TGA. PEI and HMDA functionalized silica-bead exhibited CO_2 capture capacity of 5.7 wt% (1.29 mmol g^{-1}, N contents 12 wt%) and 4 wt% (0.90 mmol g^{-1}, N-contents 9.9 wt%), respectively (Fig. 4 and Table S2†). Preliminary analysis indicated that PEI silica-bead showed higher CO_2 capture capacity despite fewer primary amines compared to HMDA which could be due to better diffusion, and accessibility of active sites.

The adsorption of amine and formation of different CO_2-amine chemical species in pellets were confirmed by FTIR. Before FTIR measurements, pellets are degassed at RT and

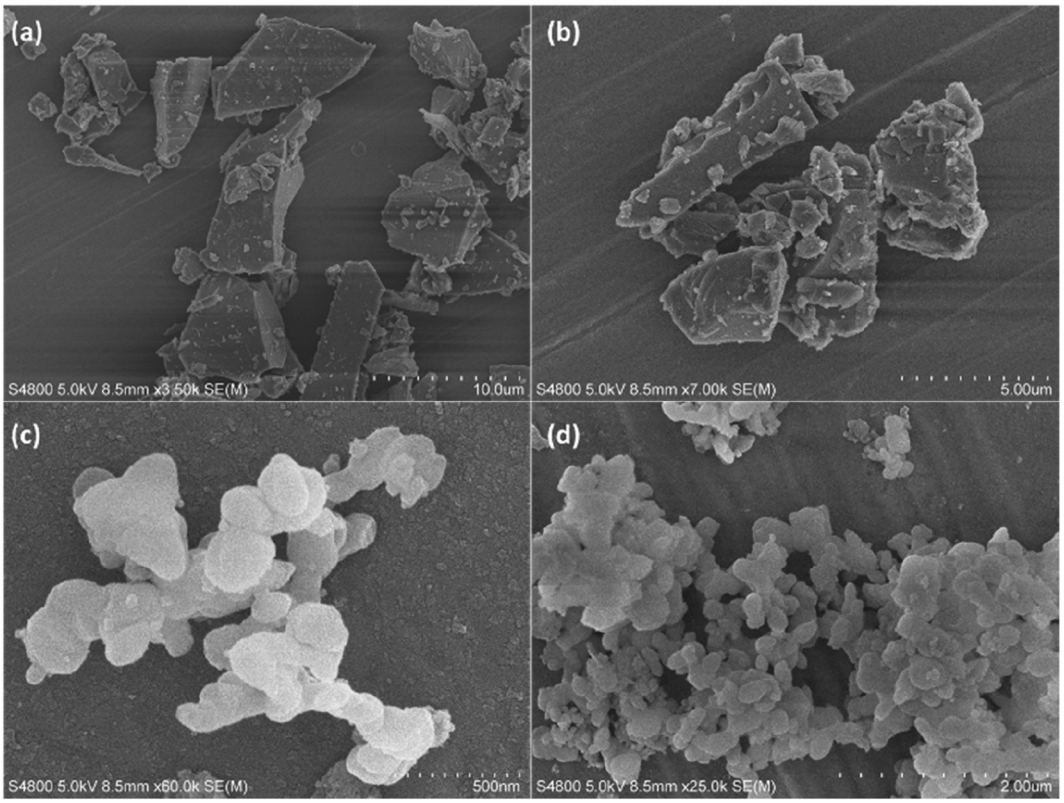

Fig. 3 SEM images of (a and b) BFS, (c and d) Silica.

saturated with CO_2 overnight in a closed chamber. Powder samples were used to measure FTIR. The presence of PEI and HMDA in beads was confirmed by adsorption features in the range of 3000–2500, and 1500–1000 cm^{-1} (Fig. S13†). After CO_2 adsorption, the spectrum indicated the presence of CO_2 species in the samples, NH stretching was observed at 3280 cm^{-1}, and with corresponding NH bending in the region of 1100–1800 cm^{-1}.[65] The absorption band on the region 1500–1200 cm^{-1} was attributed to chemical species formed when CO_2 reacts with amines, the peak at 1560 cm^{-1} assigned to stretching band of carbamate (COO^-). Peaks at 1404 cm^{-1}, and 1376 cm^{-1} were attributed to NH_2^+ deformation of secondary amine and C–N stretching/$NCOO^-$ skeleton vibration of carbamate.[65] In FTIR spectra of pellets, typical peaks of sodium alginates were much weaker than pure alginate powder, suppressed and superimposed by amine-CO_2 chemical species in pellets.

Kinetics of CO_2 adsorption. To gain a deeper understanding of the CO_2 adsorption and desorption kinetics of PEI/HMDA functionalized beads, we systematically evaluated the time-dependent behaviour of adsorbents at different temperatures and flow rates under the typical 15% CO_2 in N_2 conditions. Initially, three kinetic models, Pseudo first order (eqn (1)),[66] Pseudo second order (eqn (2)),[67] and Avrami kinetic models (eqn (3)) were applied to fit the experimental TGA adsorption data.[68–70] From this analysis, the most predictable model was selected and utilized for further analysis of the best sample (silica-PEI), recognizing the different kinetic models can explain different CO_2 adsorption mechanisms.[71]

The experimental CO_2 adsorption TGA profiles and corresponding fitting curves for silica-PEI and silica-HMDA are illustrated in Fig. 5 and relative parameters obtained after kinetic modelling are summarized in respective Table 1. The Pseudo first order kinetic model did not fit entirely the CO_2 adsorption profile (Fig. 5a); however, it provides a good fit for the initial CO_2 capture profile. Conversely, Pseudo second order (Fig. 5b) and Avrami kinetic models (Fig. 5c) demonstrated good fits across almost the entire CO_2 adsorption profile.

Among the three kinetic models, the Avrami kinetic model accurately predicted Q_e value of 1.28 which closely matched the experimental values of 1.29 for silica-PEI. Silica-HMDA showed a higher k_A compared to silica-PEI despite having a lower CO_2 adsorption capacity. This suggests that primary amine groups are highly reactive compared to secondary amines, as most of the amines in PEI are secondary. This difference in adsorption capacity could be due to the accessibility of CO_2 capture sites, sites, and better diffusion of CO_2 within the silica-PEI.

Effect of adsorption temperature and CO_2 flow rate. The Silica-PEI beads were further investigated for the effect of CO_2 flow rate and adsorption temperature to determine suitable conditions (Fig. 6). With increasing adsorption temperature, the CO_2 adsorption capacity of silica-PEI bead increased from 2.8 wt% (0.63 mmol g^{-1}) at 30 °C to 5.2 wt% (1.18 mmol g^{-1})

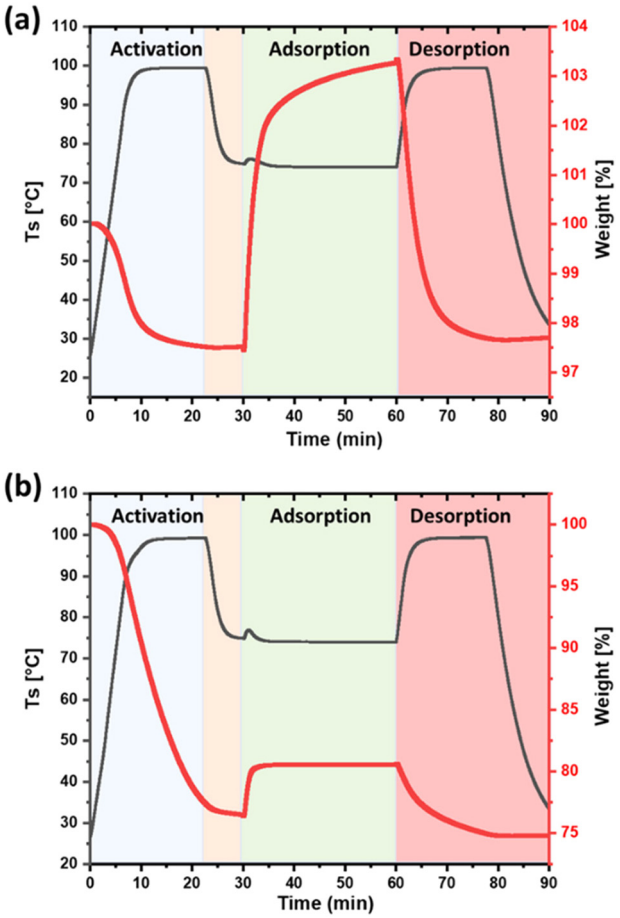

Fig. 4 CO_2 adsorption on (a) silica-PEI bead and (b) silica-HMDA bead. Adsorption at 75 °C for 30 min, using 15% CO_2 in N_2, desorption at 100 °C for 15 min.

at 75 °C and decreased to 4.9 wt% (1.11 mmol) as temperature rose to 90 °C (Fig. 6a and S14†). This trend can be attributed to increased mobility of amines, change in amine distribution due to high temperature, enhanced CO_2 diffusion, increased accessibility of amine sites at higher adsorption temperatures,

Table 1 Kinetic parameters of various kinetic models for silica-PEI and silica-HMDA bead

Kinetic Model	Parameters	Silica-PEI	Silica-HMDA
Pseudo first order	Q_e	1.25 ± 0.001	0.940 ± 0.0002
	k_1	0.400 ± 0.002	1.16 ± 0.004
	R^2	0.9879	0.9899
Pseudo second order	Q_e	1.38 ± 0.001	0.972 ± 0.001
	k_2	0.432 ± 0.002	2.54 ± 0.042
	R^2	0.9999	0.9999
Avrami	Q_e	1.28 ± 0.001	0.938 ± 0.0002
	k_A	0.396 ± 0.002	1.12 ± 0.002
	n_A	0.767 ± 0.004	1.21 ± 0.005
	R^2	0.9999	0.9999

and improved selectivity toward CO_2 over N_2.[72,73] However, at 90 °C, the CO_2 capture capacity decreased to 1.11 mmol g^{-1}, possibly due to the equilibrium between amine and CO_2 shifting to the left side (favoured desorption more).[73,74] At lower temperatures, the thermal stability of chemical species formed by a chemical reaction between amine and CO_2 is stronger than the desorption temperatures. Higher adsorption temperature closer to desorption conditions leads to decreased thermal stability of chemical species and a shift in equilibrium towards lower values.[57]

At 75 °C, a suitable adsorption temperature was identified for further analysis, and the effect of CO_2 flow rate was optimized at 75 °C (Fig. S15†). Interestingly, the lowest flow (25 mL min^{-1}) exhibited a higher CO_2 adsorption capacity compared to flow rates of 50, 75, and 100 mL min^{-1}, indicating that the bead achieved saturation within a short period (Fig. 6b and S15†). The rate constant k_A increased with temperature and decreased at 90 °C (Table 2). This is supported by the higher k_A values observed at various flow rates, indicating that the amine sites are highly accessible and saturate rapidly even at a low CO_2 flow rate (25 mL min^{-1}). Additionally, the n_A value varied with different adsorption temperatures and flow rates, predicting that the CO_2 adsorption mechanism was different for each system (Table 2). The CO_2 diffusion rate and mass transfer rate significantly influence the adsorbent's CO_2 adsorption performance, and rapid saturation and desorption

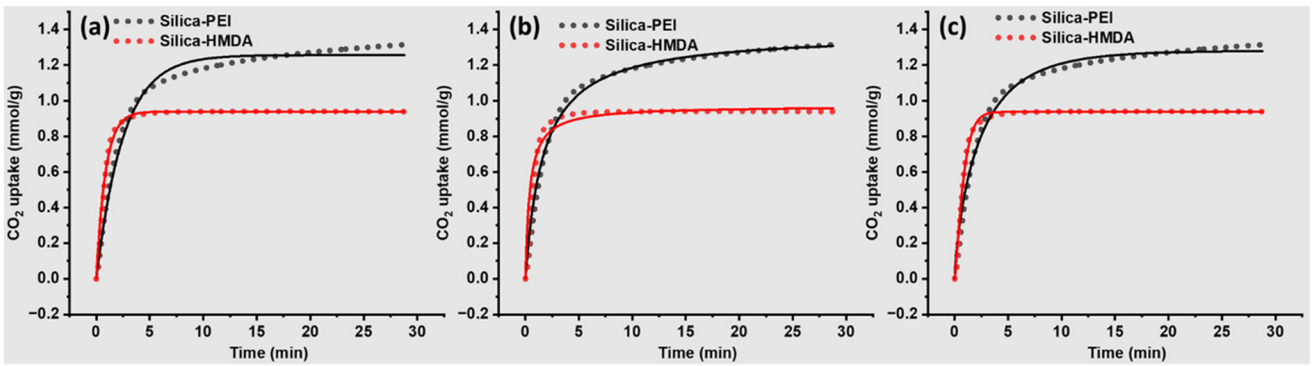

Fig. 5 Fitting of CO_2 adsorption profiles using three kinetic models, (a) Pseudo first order kinetic model, (b) Pseudo second order, and (c) Avrami kinetic model.

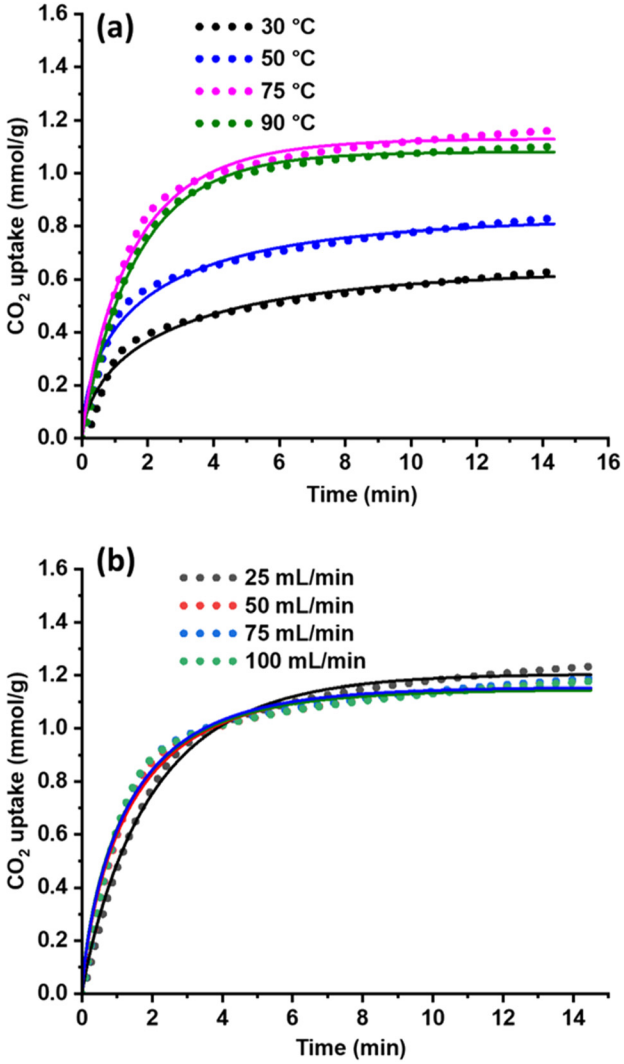

Fig. 6 Effect of adsorption temperature (a) and CO_2 flow rates (b) on CO_2 capture capacity and their corresponding Avrami model fitted curves of silica-PEI bead.

are favourable for the large-scale deployment of such adsorbents.

Desorption of CO_2. Desorption is a critical stage in adsorbent design and large-scale applications. Achieving a low desorption temperature and high rate of CO_2 desorption/regeneration is crucial for the widespread deployment of CO_2 capture technology with reduced cost. To this end, four different desorption temperatures (90, 100, 110, and 120 °C) were selected to regenerate silica-PEI bead (Fig. 7 and S16†).

As the desorption temperature increased, the rate of desorption (k_A) also increased (Table S3†), and the bead desorbed quickly within 10 min (Fig. 7a). However, at 90 °C, the bead took a considerably longer time compared to the other desorption temperatures, reflecting the thermal stability of chemical species formed during the CO_2 adsorption (Fig. 7a). These observations indicate that the beads were easily and fully regenerable within the range of 90–120 °C, as supported by the $-Q_e$ values (Fig. 7b). However, it is essential to note that higher temperatures could lead to amine degradation, leaching, and formation of stable chemical species.[75–77] Therefore, 100 °C for 15 min was selected for further investigation to minimize thermal degradation and amine leaching.

Diffusion limitations within beads were also accessed by converting the bead into powder and using them for CO_2 capture investigations. Corresponding PEI powder samples showed similar CO_2 capture capacity as beads (Fig. S17†). The Avrami kinetic models of powder samples also revealed higher k_A values for both adsorption (*i.e.* 0.90) and desorption (*i.e.* 0.65) compared to beads (*i.e.* 0.36, and 0.37 for adsorption and desorption, respectively) (Fig. S17, S18 and Tables S4, S5†). This indicates that both CO_2 adsorption and desorption are diffusion-limited in beads.

Adsorption–desorption cycles. The recyclability of solid adsorbents is crucial, and we conducted 105 adsorption–desorption cycles and observed a continuous reduction in adsorption capacity (Fig. 8 and S19†). Silica-HMDA exhibited a gradual decrease in CO_2 adsorption capacity (Fig. 8 and S20†), and experienced a 50% reduction just in 20 cycles, primarily due to the vaporization/degradation of HMDA. The formation of stable chemical species such as urea, or cyclic urea type species may also increase the rate of adsorbent degradation with no. of cycles.[78–80] The degradation mechanism has been investigated previously, highlighting the importance of understanding and mitigating adsorbent degradation in long-term applications.[79,81–83]

Table 2 Fitting parameter of Avrami kinetic model for the adsorption of CO_2 on silica-PEI bead

	Parameters	30 °C	50 °C	75 °C	90 °C
Effect of temperature	Q_e	0.64 ± 0.004	0.83 ± 0.003	1.13 ± 0.001	1.08 ± 0.001
	k_A	0.371 ± 0.008	0.510 ± 0.008	0.634 ± 0.003	0.599 ± 0.002
	n_A	0.625 ± 0.009	0.596 ± 0.007	0.854 ± 0.007	0.935 ± 0.004
	R^2	0.9999	0.9999	0.9999	0.9999
Effect of flow		25 mL min^{-1}	50 mL min^{-1}	75 mL min^{-1}	100 mL min^{-1}
	Q_e	1.20 ± 0.001	1.15 ± 0.001	1.15 ± 0.001	1.14 ± 0.001
	k_A	0.489 ± 0.002	0.678 ± 0.004	0.708 ± 0.005	0.725 ± 0.005
	n_A	0.904 ± 0.005	0.773 ± 0.006	0.771 ± 0.007	0.757 ± 0.006
	R^2	0.9999	0.9999	0.9999	0.9999

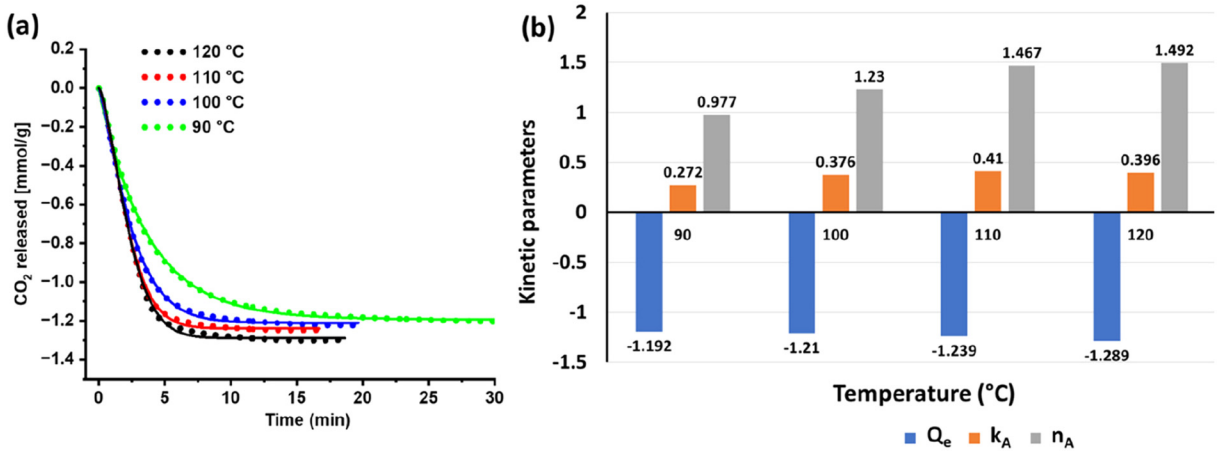

Fig. 7 (a) Desorption temperature optimization using Silica-PEI bead. (b) Kinetic parameters of four different desorption temperatures.

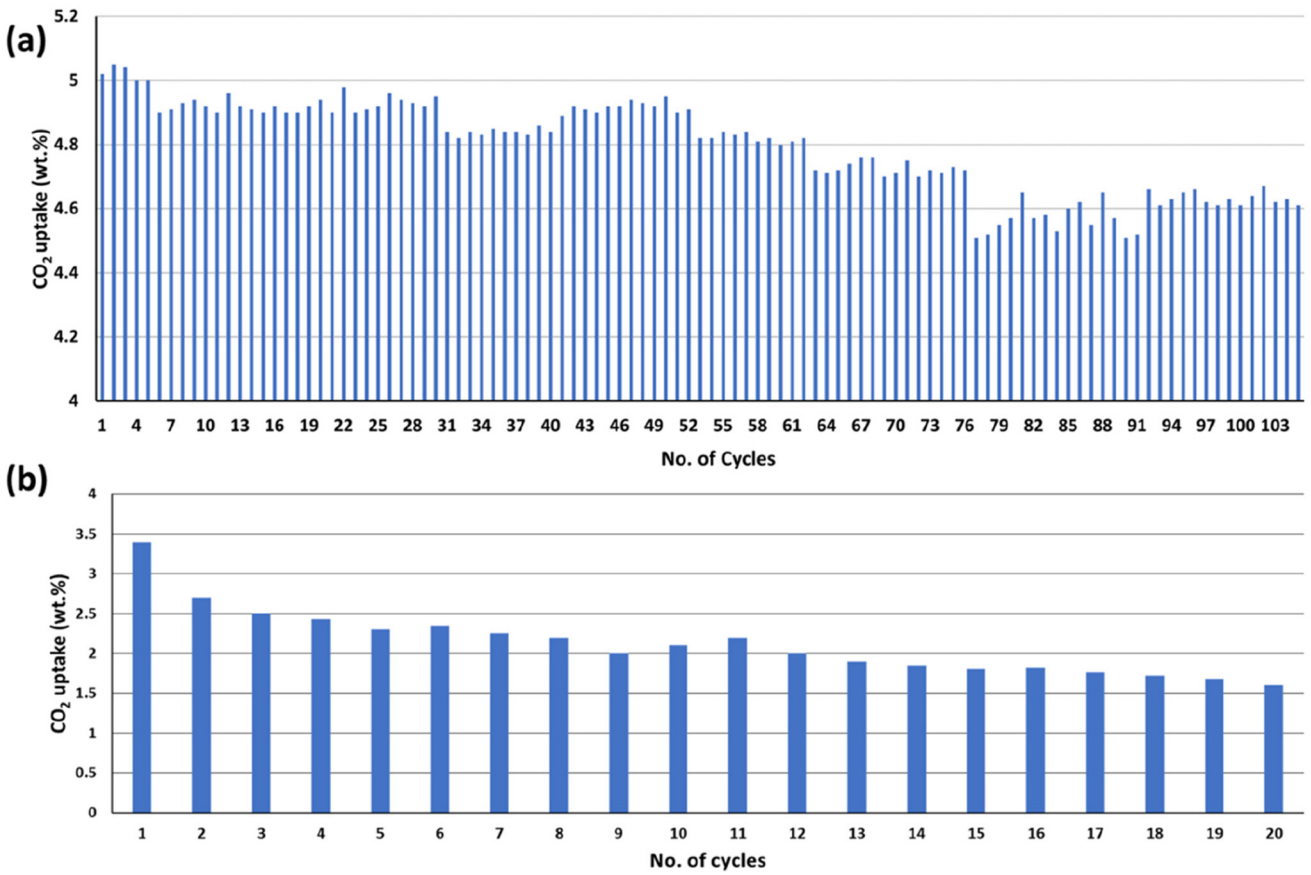

Fig. 8 (a) 105 adsorption–desorption cycles of silica-PEI bead. (b) 20 adsorption–desorption cycles of silica-HMDA bead. Adsorption was performed at 75 °C, a CO_2 flow rate of 25 mL min^{-1} for 15 min, and desorption at 100 °C for 15 min under the flow of N_2 (50 mL min^{-1}).

Conclusion

We have successfully demonstrated the viability of utilizing BFS, a steel industrial waste abundant in supply, for the synthesizing mesoporous silica, employing a two-stage dissolution and precipitation using HCl and NaOH. The prepared mesoporous silica possesses a moderate surface area of 100 m^2 g^{-1} and a wide pore size distribution ranging from 4–20 nm. Our investigation highlights the potential to explore BFS for the continuous production of mesoporous silica using dissolution-precipitation at a large scale.

Furthermore, we converted the mesoporous silica powder into industrial-grade solid amine adsorbents and evaluated their performance for CO_2 capture (15% CO_2 in N_2). PEI functionalized silica bead demonstrated superior performance compared to HMDA. After 105 adsorption–desorption cycles, the silica-PEI bead revealed no significant sign of performance degradation (approximately 8% decrease in adsorption capacity was observed). It's essential to note for the practical applications, making beads/pellets/monoliths a more feasible and scalable option for industries.

Author contributions

Conceptualization, analysis, methodology, validation, visualization, writing original draft and management: BS; SEM and elemental analysis: BS and MK; review, and editing: MK, JY, TR.

Data availability

The Authors confirm that the data supporting the findings of this study are available within the article and ESI.†

Conflicts of interest

The authors declare no competing financial interest.

Acknowledgements

B. S and T. R. are grateful for financial support from Business Finland 8205/31/2022. We would like to thank Dr. Risto Koivula for helping us with N_2 sorption analysis.

References

1 M. Barreiro-Gen and R. Lozano, *Bus. Strategy Environ.*, 2020, **29**, 3484–3494.
2 P. Schroeder, K. Anggraeni and U. Weber, *J. Ind. Ecol.*, 2019, **23**, 77–95.
3 Y. Jiang, P. Tan, S.-C. Qi, X.-Q. Liu, J.-H. Yan, F. Fan and L.-B. Sun, *Angew. Chem., Int. Ed.*, 2019, **58**, 6600–6604.
4 N. Yuan, A. Zhao, Z. Hu, K. Tan and J. Zhang, *Chemosphere*, 2022, **287**, 132227.
5 G. A. Khater, B. S. Nabawy, A. A. El-Kheshen, M. Abdel-Baki and M. M. Farag, *Mater. Chem. Phys.*, 2022, **280**, 125784.
6 W. Liu, Y. Wang, J. Li and B. Li, *Int. J. Appl. Ceram. Technol.*, 2023, **20**, 3584–3595.
7 D. M. Proctor, K. A. Fehling, E. C. Shay, J. L. Wittenborn, J. J. Green, C. Avent, R. D. Bigham, M. Connolly, B. Lee, T. O. Shepker and M. A. Zak, *Environ. Sci. Technol.*, 2000, **34**, 1576–1582.
8 A. J. Hobson, D. I. Stewart, A. W. Bray, R. J. G. Mortimer, W. M. Mayes, M. Rogerson and I. T. Burke, *Environ. Sci. Technol.*, 2017, **51**, 7823–7830.
9 Q. Zeng, X. Liu, Z. Zhang, C. Wei and C. Xu, *Green Energy Resour.*, 2023, **1**, 100012.
10 W. M. Mayes, A. L. Riley, H. I. Gomes, P. Brabham, J. Hamlyn, H. Pullin and P. Renforth, *Environ. Sci. Technol.*, 2018, **52**, 7892–7900.
11 E. Özbay, M. Erdemir and H. İ. Durmuş, *Constr. Build. Mater.*, 2016, **105**, 423–434.
12 X. Chen, Y. He, X. Cui and L. Liu, *Fuel*, 2023, **338**, 127309.
13 H. Pullin, A. W. Bray, I. T. Burke, D. D. Muir, D. J. Sapsford, W. M. Mayes and P. Renforth, *Environ. Sci. Technol.*, 2019, **53**, 9502–9511.
14 M. Seggiani and S. Vitolo, *Resour., Conserv. Recycl.*, 2003, **40**, 71–80.
15 L. Chen, S. Ren, H. Peng, J. Yang, M. Wang, Z. Chen and Q. Liu, *Appl. Catal., A*, 2022, **646**, 118868.
16 T.-S. Tran, J. Yu, C. Li, F. Guo, Y. Zhang and G. Xu, *RSC Adv.*, 2017, **7**, 18108–18119.
17 Z. Lu, Z. Lei, S. Hao, J. Yang, Z. Lei, B. Fang and C. Xiaosheng, *ACS Omega*, 2020, **5**, 32216–32226.
18 L. Zhang, Y. Han, H. Shu, L. Zhang, Z. Han, X. Yang and Y. Chen, *J. Chem. Technol. Biotechnol.*, 2023, **98**, 949–957.
19 Y. Kuwahara and H. Yamashita, *J. CO2 Util.*, 2013, **1**, 50–59.
20 Z. Lei, L. Xi, Q. Lingbo, S. Hao, J. Yang, L. Zhang, Y. Yao and B. Fang, *RSC Adv.*, 2021, **11**, 15036–15043.
21 C. Chen, S.-R. Wu and C.-T. Kao, *ACS Omega*, 2023, **8**, 47075–47085.
22 F. Qi, J. Sun, G. Zhu, H. Li, Y. Wu, S. Li, C. Yang, J. Zheng and Y. Zhang, *Process Saf. Environ. Prot.*, 2022, **165**, 1–12.
23 M. S. Barbarey, M. M. El-Sayed Seleman, A. A. El Kheshen and M. F. Zawrah, *Constr. Build. Mater.*, 2024, **411**, 134226.
24 W. Ren, P. Zhou, Y. Tian, W. Wang, Y. Dong, T. Wang, L. Zhang, C. Ma and X. Zhao, *Appl. Catal., A*, 2020, **606**, 117810.
25 G. Hu, S. Rohani, X. Jiang, J. Li, Q. Liu and W. Liu, *ACS Sustainable Chem. Eng.*, 2021, **9**, 13963–13971.
26 C.-F. Liu and S.-M. Shih, *Environ. Sci. Technol.*, 2004, **38**, 4451–4456.
27 Y. H. Lee, H. Eom, S. M. Lee and S. S. Kim, *RSC Adv.*, 2021, **11**, 8306–8313.
28 V. Trinkel, O. Mallow, C. Thaler, J. Schenk, H. Rechberger and J. Fellner, *Ind. Eng. Chem. Res.*, 2015, **54**, 11759–11771.
29 Y. Kuwahara, A. Hanaki and H. Yamashita, *ACS Sustainable Chem. Eng.*, 2022, **10**, 372–381.
30 M. Owais, M. Järvinen, P. Taskinen and A. Said, *J. CO_2 Util.*, 2019, **31**, 1–7.
31 J. Yu and K. Wang, *Energy Fuels*, 2011, **25**, 5483–5492.
32 S. Tian, J. Jiang, F. Yan, K. Li and X. Chen, *Environ. Sci. Technol.*, 2015, **49**, 7464–7472.
33 L. Chen, S. Ren, X. Xing, J. Yang, J. Yang, M. Wang, Z. Chen and Q. Liu, *ACS Sustainable Chem. Eng.*, 2022, **10**, 7739–7751.
34 Y. Kuwahara, K. Tsuji, T. Ohmichi, T. Kamegawa, K. Mori and H. Yamashita, *ChemSusChem*, 2012, **5**, 1523–1532.

35 Y. Kuwahara, S. Tamagawa, T. Fujitani and H. Yamashita, *J. Mater. Chem. A*, 2013, **1**, 7199–7210.
36 Y. Kuwahara, A. Hanaki and H. Yamashita, *Green Chem.*, 2020, **22**, 3759–3768.
37 N. Shekhar Samanta, P. P. Das, S. Dhara and M. K. Purkait, *Ind. Eng. Chem. Res.*, 2023, **62**, 9006–9031.
38 M. Oge, D. Ozkan, M. B. Celik, M. Sabri Gok and A. Cahit Karaoglanli, *Mater. Today: Proc.*, 2019, **11**, 516–525.
39 W. Duan, Q. Yu, J. Liu, L. Hou, H. Xie, K. Wang and Q. Qin, *Appl. Therm. Eng.*, 2016, **98**, 936–943.
40 Y. W. Chiang, R. M. Santos, J. Elsen, B. Meesschaert, J. A. Martens and T. Van Gerven, *Chem. Eng. J.*, 2014, **249**, 260–269.
41 J. Xiao, F. Li, Q. Zhong, H. Bao, B. Wang, J. Huang and Y. Zhang, *Hydrometallurgy*, 2015, **155**, 118–124.
42 E. A. Gorrepati, P. Wongthahan, S. Raha and H. S. Fogler, *Langmuir*, 2010, **26**, 10467–10474.
43 B. Rao, H. Dai, L. Gao, H. Xie, G. Gao, K. Peng, M. Zhang, F. He and Y. Pan, *J. Cleaner Prod.*, 2022, **341**, 130779.
44 R. Dupuis, R. Pellenq, J.-B. Champenois and A. Poulesquen, *J. Phys. Chem. C*, 2020, **124**, 8288–8294.
45 M. Fertani-Gmati, K. Brahim, I. Khattech and M. Jemal, *Thermochim. Acta*, 2014, **594**, 58–67.
46 F. K. Crundwell, *ACS Omega*, 2017, **2**, 1116–1127.
47 A. Pohl, *Water, Air, Soil Pollut.*, 2020, **231**, 503.
48 J. Hwang, J. H. Lee and J. Chun, *Mater. Lett.*, 2021, **283**, 128765.
49 K. Kosuge, N. Kikukawa and M. Takemori, *Chem. Mater.*, 2004, **16**, 4181–4186.
50 M. Hessien and E. Prouzet, *ChemistrySelect*, 2021, **6**, 1440–1447.
51 N. Bayal, B. Singh, R. Singh and V. Polshettiwar, *Sci. Rep.*, 2016, **6**, 24888.
52 A. Samanta, A. Zhao, G. K. H. Shimizu, P. Sarkar and R. Gupta, *Ind. Eng. Chem. Res.*, 2012, **51**, 1438–1463.
53 J. Wang, L. Huang, R. Yang, Z. Zhang, J. Wu, Y. Gao, Q. Wang, D. O'Hare and Z. Zhong, *Energy Environ. Sci.*, 2014, **7**, 3478–3518.
54 M. Bisht, Bhawna, B. Singh and S. Pandey, *J. Mol. Liq.*, 2023, **384**, 122203.
55 B. Singh and V. Polshettiwar, *J. Mater. Chem. A*, 2016, **4**, 7005–7019.
56 B. Singh, J. Na, M. Konarova, T. Wakihara, Y. Yamauchi, C. Salomon and M. B. Gawande, *Bull. Chem. Soc. Jpn.*, 2020, **93**, 1459–1496.
57 B. Singh and V. Polshettiwar, *Pure Appl. Chem.*, 2023, **95**, 451–462.
58 B. Singh and V. Polshettiwar, *Nanoscale*, 2019, **11**, 5365–5376.
59 B. Singh, A. Maity and V. Polshettiwar, *ChemistrySelect*, 2018, **3**, 10684–10688.
60 C. Chen, S.-T. Yang, W.-S. Ahn and R. Ryoo, *Chem. Commun.*, 2009, 3627–3629.
61 D. Zabiegaj, M. Caccia, M. E. Casco, F. Ravera and J. Narciso, *J. CO_2 Util.*, 2018, **26**, 36–44.
62 S. Yang, L. Peng, O. A. Syzgantseva, O. Trukhina, I. Kochetygov, A. Justin, D. T. Sun, H. Abedini, M. A. Syzgantseva, E. Oveisi, G. Lu and W. L. Queen, *J. Am. Chem. Soc.*, 2020, **142**, 13415–13425.
63 K. Maresz, A. Ciemięga, J. J. Malinowski and J. Mrowiec-Białoń, *Chem. Eng. J.*, 2020, **383**, 123175.
64 M. A. Sakwa-Novak, C.-J. Yoo, S. Tan, F. Rashidi and C. W. Jones, *ChemSusChem*, 2016, **9**, 1859–1868.
65 J. Yu and S. S. C. Chuang, *Energy Fuels*, 2016, **30**, 7579–7587.
66 E. D. Revellame, D. L. Fortela, W. Sharp, R. Hernandez and M. E. Zappi, *Clean. Eng. Technol.*, 2020, **1**, 100032.
67 V. K. Singh and E. A. Kumar, *Energy Procedia*, 2016, **90**, 316–325.
68 Q. Liu, J. Shi, S. Zheng, M. Tao, Y. He and Y. Shi, *Ind. Eng. Chem. Res.*, 2014, **53**, 11677–11683.
69 M. Songolzadeh, M. Soleimani and M. Takht Ravanchi, *J. Nat. Gas Sci. Eng.*, 2015, **27**, 831–841.
70 B. Guo, Y. Wang, X. Qiao, X. Shen, J. Guo, J. Xiang and Y. Jin, *Chem. Eng. J.*, 2021, **421**, 127865.
71 H. Chen, S. Dong, Y. Zhang and P. He, *Energy*, 2022, **239**, 122348.
72 F. Rezaei, R. P. Lively, Y. Labreche, G. Chen, Y. Fan, W. J. Koros and C. W. Jones, *ACS Appl. Mater. Interfaces*, 2013, **5**, 3921–3931.
73 Y. Fan and X. Jia, *Energy Fuels*, 2022, **36**, 1252–1270.
74 J. J. Lee, C. Sievers and C. W. Jones, *Ind. Eng. Chem. Res.*, 2019, **58**, 22551–22560.
75 A. I. Balabanovich, I. A. Klimovtsova, V. P. Prokopovich and N. R. Prokopchuk, *Thermochim. Acta*, 2007, **459**, 1–8.
76 G. T. Rochelle, *Curr. Opin. Chem. Eng.*, 2012, **1**, 183–190.
77 A. Azarpour and S. Zendehboudi, *ACS Omega*, 2023, **8**, 26850–26870.
78 R. A. Khatri, S. S. C. Chuang, Y. Soong and M. Gray, *Energy Fuels*, 2006, **20**, 1514–1520.
79 J. S. A. Carneiro, G. Innocenti, H. J. Moon, Y. Guta, L. Proaño, C. Sievers, M. A. Sakwa-Novak, E. W. Ping and C. W. Jones, *Angew. Chem., Int. Ed.*, 2023, **62**, e202302887.
80 Q. T. Vu, H. Yamada and K. Yogo, *Ind. Eng. Chem. Res.*, 2021, **60**, 4942–4950.
81 C. S. Srikanth and S. S. C. Chuang, *ChemSusChem*, 2012, **5**, 1435–1442.
82 C. Xu, Y. Zhang, Y.-L. Peng, T. Yang, Z. Liu, F. Qiu, A. Oloruntoba and S. Jiang, *Sep. Purif. Technol.*, 2024, **331**, 125621.
83 Q. T. Vu, H. Yamada and K. Yogo, *Energy Fuels*, 2019, **33**, 3370–3379.